EPJ manuscript No.
(will be inserted by the editor)

Ratchet rotation of a 3D dimer on a vibrating plate

Jiao Wang[1] and Caishan Liu[1,a] and Yan-Bin Jia[2] and Daolin Ma[1]

[1] State Key Laboratory for Turbulence and Complex Systems, College of Engineering, Peking University, Beijing 100871, China
[2] Department of Computer Science, Iowa State University, Ames, IA 50011, USA

Received: date / Revised version: date

Abstract. This work studies the dynamics of a 3D dimer bouncing upon a horizontal plate undergoing a vertical harmonic vibration. Despite complex interactions within the system due to impacts and friction, numerical simulation shows that, under certain conditions prescribed for the dynamics, the center of mass of the dimer, when projected onto a horizontal plane, will follow a *circular orbit*. The phenomenon is like a particle under Coulomb friction performing a ratchet motion that rotates around. Investigations further reveal that the dimer dynamics bear some typical characteristics of a nonlinear system, including sensitivity to the initial conditions and bifurcation behaviors related to the physical parameters of the dynamics. Our results indicate that the coefficient of restitution and the plate's vibration intensity play critical roles in exciting the circular orbit, while the dimer's geometry and the vibration frequency mainly influence the trajectory characteristics. These findings may help understand transport mechanisms underlying systems of granular matter with anisotropic particles.

PACS. 05.45.-a Nonlinear dynamics – 45.50.Tn Classical mechanics – 45.70.-n Granular systems, classical mechanics of – 79.20.Ap Computer modeling and simulation of impact phenomena, solids

1 Introduction

Recently, considerable attention has been paid to granular material because of its complex properties in physics [1,2]. For instance, under an external excitation granular material can exhibit self-organization [3–5], which leads to the formation of large vortices [4,5], cluster phenomena [6], directed transport of particles [7–11], *etc*. Similar ordered behaviors are also leveraged by a passive walker to perform different gaits [12,13] or by a robot juggler to converge the initial free flight of an object into a vertical periodic motion [14]. These unusual emerging properties might seem, at first glance, to contradict our physical intuition, but indeed manifest strong nonlinearities in the asymmetric structures of the spatiotemporal responses to generate self-organized behaviors.

To clarify the diversity of dynamics subjected to external perturbations, a single particle is used in most studies in the physics community [15–25]. A driven particle, with periodic potential and under frictional force and thermal fluctuations, can exhibit rich nonlinear behaviors including periodic structures [17,18], period-doubling bifurcation [19], chattering mechanism [20,21], chaos [20,22,23], *etc*. Even though crucial clues have been revealed to the mechanism underlying the aforementioned behaviors [15,16], an idealized one-dimensional particle model does not envelope all the characteristics of dynamics as exhibited by granular materials and robotic systems. This has prompted the study of the roles of geometry in the above systems [26–33].

To discover the influence by the particle shape on a transfer mechanism in stochastic dynamics, Atwell *et. al* [29] studied the anisotropic dynamics of a shaken granular dimer, and detailed the similarities and differences in its dynamics behaviors from those of monomer species. Systematic investigation into stochastic dynamics of a bouncing rod [30] revealed that the rod dynamics could change from being periodic or near periodic to being stochastic as vibration intensifies. Anomalous behaviors agitated by rod-shaped grains were also found in an experiment recently performed in an microgravity environment [33].

Focusing on a specific scenario of vibration with lower energy, Dorbolo *et. al* [28] experimentally and numerically studied the dynamics of a dimer bouncing on an oscillating plate. They showed that the bouncing dimer displayed spontaneous symmetry breaking to generate periodic responses that could be classified into three modes: *drift*, *jump*, and *flutter*.

All the work mentioned above indicates that collision and friction are responsible for the transfer of energy and momentum, and therefore require proper characterization in the modeling of granular systems. Usually, numerical simulation can be performed using a simplified molecular dynamics (MD) technique which adopts a stiffness-centered parameter to represent material elasticity, plus a damping coefficient to quantify dissipation of energy [30,34–36]. Although capable of capturing main motion features, an MD technique often requires parameters that have to be determined via fitting subject to constraints imposed by practical requirements. This is usually impossible in real physics, and would cause relative large discrepancies between the predicted scenarios and reality [36]. Moreover, when

[a] *email:* liucs@pku.edu.cn

numerical results are obtained from a MD technique, the periodic characteristics of systems may be easily lost due to the mixture of information on different scales.

To avoid the disadvantages of MD models, we recently developed a new approach to solving impact problems with and without friction [38,41]. In this model, material behaviors due to impact are described by a force-energy relationship between the contact force and the elastic potential energy. This relationship is mathematically deduced from the force-deformation relations specific to materials. Note that the elastic potential energy at a contact point is transferred from the work done by the contact force via elastic deformation. Meanwhile, the work can be equally determined by integrating the normal relative velocity over the normal impulse. Accumulation of the elastic potential energy can then be obtained based on the work, together with an energetic coefficient to scale its dissipation in the work-to-energy transition. At any instant this presents an instantaneous distribution for the potential energy in all contact points, and then for the normal contact forces by the force-energy relationship. Therefore, we can replace the time scale in impact dynamics with an independent impulse scale, and describe the impact dynamics as a model of first order dynamics with respect to a "time-like" independent impulse. This model avoids the numerical difficulties suffered by an MD model, due to integration over a small time period. It adopts parameters that can be experimentally measured [41]. The numerical results obtained from this method can achieve good agreements in comparison with experimental findings [39–42].

Based on the recent development in nonsmooth dynamics, Zhao *et. al* [37] numerically and theoretically studied the dynamics of a bouncing dimer. Good agreements were achieved between their numerical results and experimental findings from [28]. Obtained by the same approach from [38] to model a 3D bouncing dimer, our recent results [43] indicated that the dimer's 3D motion has the same three modes (*drift*, *flutter*, *jump*) as discovered for the 2D version. However, these modes in 3D correspond to distinct transport mechanisms. Possible trajectories of the dimer's center of mass projected onto the horizontal plane include a *circular orbit*, a *dog-leg path*, and a *straight line* in the *drift*, *flutter*, and *jump* modes, respectively. This paper aims at investigating physical properties of the circular orbit because of its significance in the behaviors of granular systems.

Experimentally discovered in [28] and theoretically analyzed in [37], the *drift mode* in 2D dynamics originates from a concatenation of contact states describing collisions that occur at one or both ends of the dimer. More specifically, excitation of the drift mode was found to be sensitive to the initial conditions and significantly influenced by the amplitude and frequency of the plate's harmonic vibration.

To investigate the sensitivity of the 3D *drift mode* to the initial conditions and the physical parameters of the dynamics, we assign to the dimer special initial configurations with its angle of inclination being the only adjustable parameter. The angle is then altered within the scope $(0, \pi/2)$ for the study. Numerical simulation shows that, if the values of the coefficient of restitution e and the vibration intensity Γ fall into a certain region in the e-Γ plane, an initial configuration can always be found to activate a circular orbit under the drift mode regardless of the dimer geometry and the vibration frequency. Nevertheless, once the point (e, Γ) gets outside the region, it is impossible to trigger the drift mode whatever initial conditions are set. Numerical simulation also shows that variations in the values of the related friction coefficients may alter the asymmetric structure of the slip motions of both contact ends. Such changes significantly influence the behaviors of the dimer's ratchet rotation, but virtually have little effect over excitation of the 3D *drift mode*. Therefore, besides its sensitivity to the initial conditions, excitation of a drift mode is basically influenced by e and Γ. This will be investigated via numerical simulation.

Finding the characteristics of the circular orbit triggered in the drift mode has a potential implication in understanding the underlying physical mechanisms for granular transport. Analysis over our numerical results indicate that the orbit's radius and period are both nearly proportional to the square of the frequency and the cube of the distance between the centers of the dimer's two spheres. Meanwhile, the horizontal velocity has just a small effect on the radius, though a significant impact on the period. Furthermore, numerical investigation will exhibit that the orbit period may be minimized by tuning the initial horizontal velocity of the dimer, with the minimal value occurring in the situation where the dimer's spinning axis at the instant of double collisions is approximately normal to the orbit. This scenario manifests the self-adjusting mechanism of double impacts, through which appropriate energy in the vibration is extracted by the dimer to sustain a stable circle-orbit mode.

The organization of this paper is as follows. In Sect. 2, the nonsmooth dynamics of a 3D bouncing dimer system proposed in [43] are briefly reviewed with the descriptions of the contact and impact processes. In Sect. 3, we perform numerical simulations to reveal periodic structures hidden in the motion of the dimer in the drift mode. Excitation of the drift mode is investigated in Sect. 4 via comprehensive simulation to probe the effects of the initial condition and the physical parameters of the dynamics. Sect. 5 examines the characteristics of the circular orbit, via a numerical investigation. Conclusion follows in Sect. 6.

2 Nonsmooth dynamics of the bouncing dimer

In this section, we review the dynamics of the system of a bouncing dimer studied in [43], where more derivation details and equations can be found if needed. As depicted in Fig. 1, the dimer, consisting of two identical solid balls rigidly connected by a light-weight rod, falls under gravity onto a horizontal plate in vibration. The balls have mass m_b and radius r, and their centers are at the distance l apart. The rod has mass m_r, diameter D_r, and length $l - 2r$.

The plate undergoes a vertical vibration following a harmonic signal with amplitude A_z and angular frequency ω. Its distance from the equilibrium position takes the form $z_p = A_z \sin(\omega t + \phi_0)$, where ϕ_0 represents the phase angle of the vibration at time $t = 0$. The plate is massive relative to the dimer such that its motion is not influenced by their interactions.

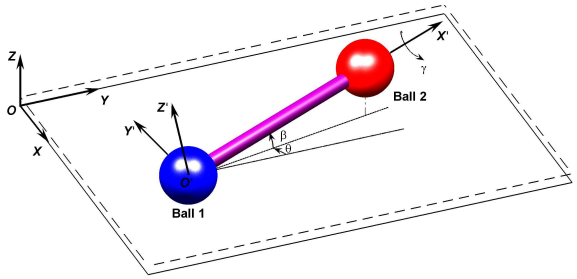

Fig. 1. (Color online) System of a dimer with two identical balls bouncing on a plate going through a harmonic vibration. The blue ball B_1 stays on the plate most of the time while the red ball B_2 is bouncing.

2.1 Dynamics and contact kinematics

We set up a base coordinate frame (O, XYZ) with the XY-plane coinciding with the plate at its equilibrium position. See Figure 1. The centers of mass of ball B_1, ball B_2, and the rod are located at (x_1, y_1, z_1), (x_2, y_2, z_2), (x_r, y_r, z_r), respectively.

We also establish a body-fixed coordinate frame $(O', X'Y'Z')$ with its X'-axis pointing from the center of B_1 to that of B_2. The attitude angles relating this frame to the base frame are θ, β, and γ, termed as the *precession*, *dip*, and *spinning* angles, respectively. The system is thus fully described by the generalized coordinates $\mathbf{q} = (x_1, y_1, z_1, \theta, \beta, \gamma)^T \in \mathbb{R}^6$.

At any instant, contacts or impacts may occur at only two points, one each on B_1 and B_2, which are the closest to the vibrating plate, among all the points on the surfaces of B_1 and B_2, respectively. We denote the instantaneous possible contact/impact point as p_1 on ball B_1 and p_2 on ball B_2, and refer to them as the *ends*. We can derive the position vectors $\mathbf{r}_1(\mathbf{q})$ and $\mathbf{r}_2(\mathbf{q})$ for the points p_1 and p_2, respectively, in the base frame. Differentiation of these two vectors gives us the normal components $v_1^n(\mathbf{q}, \dot{\mathbf{q}})$ and $v_2^n(\mathbf{q}, \dot{\mathbf{q}})$ of the velocities of the two points along the Z-axis.

Let δ_i, $i = 1, 2$, be the normal displacement of p_i relative to its potential contact point p_i' on the vibrating plane. Whenever ambiguity does not arise, we may refer to p_i and p_i' together or separately as one contact. Writing $\boldsymbol{\delta} = (\delta_1, \delta_2)^T$, we then obtain its time rate:

$$\dot{\boldsymbol{\delta}} = [v_1^n - \dot{z}_p, v_2^n - \dot{z}_p]^T = \boldsymbol{W}^T(\mathbf{q})\dot{\mathbf{q}} - (\dot{z}_p, \dot{z}_p)^T. \tag{1}$$

Expression of $\boldsymbol{W}(\mathbf{q})$ is given in Appendix A. Similarly, the tangential velocities $\boldsymbol{v}^\tau$ at the two contacts can be obtained.

To describe the interaction at each contact under Coulomb friction, we decompose the contact force along its normal and two orthogonal tangential directions. Aggregate the normal and tangential components at the two contacts separately: $\boldsymbol{F}^n = [F_1^n, F_2^n]^T$ and $\boldsymbol{F}^\tau = [F_{1x}^\tau, F_{2x}^\tau, F_{1y}^\tau, F_{2y}^\tau]^T$. Writing out the dimer's kinetic and potential energies, we apply the Euler-Lagrange equations to obtain the system dynamics as follows:

$$\boldsymbol{M}(\mathbf{q})\,\ddot{\mathbf{q}} - \boldsymbol{h}(\mathbf{q}, \dot{\mathbf{q}}, t) = \boldsymbol{Q} + \boldsymbol{W}\boldsymbol{F}^n + \boldsymbol{N}\boldsymbol{F}^\tau, \tag{2}$$

where the matrices $\boldsymbol{M}(\mathbf{q})$, $\boldsymbol{h}(\mathbf{q}, \dot{\mathbf{q}}, t)$, $\boldsymbol{Q}$, and $\boldsymbol{N}$ are given in Appendix A. The above equation describes $\ddot{\mathbf{q}}$ in terms of $\mathbf{q}$ and $\dot{\mathbf{q}}$, and requires conditions to determine the unknown contact forces.

Below we introduce three groups of complementarity conditions to describe the contact interactions. The first group is concerned with the normal displacements at the potential contact p_i, $i = 1, 2$:

$$\delta_i(t) \cdot F_i^n(t) = 0,\ \delta_i(t) \geq 0,\ F_i^n(t) \geq 0. \tag{3}$$

Clearly, a disengaged contact ($\delta_i(t) > 0$) admits zero interaction force ($F_i^n(t) = 0$).

In case of $\delta_i(t) = 0$, we should resort to a second group of complementarity conditions at the velocity level generated from (3) by replacing $\delta_i(t)$ with $\dot{\delta}_i(t)$. When $\delta_i(t) = 0$ and $\dot{\delta}_i(t) < 0$, an impact is triggered at the point p_i. Section 2.2 will present a method for obtaining the post-impact outputs.

In case of $\delta_i(t) = 0$ and $\dot{\delta}_i(t) = 0$, we need to look at the second derivative. In (3), simply replace $\delta(t)$ with $\ddot{\delta}_i(t)$, which can be obtained by differentiating (1).

Coulomb's friction law characterizes the tangential interactions on a rough surface. In the dimer problem, we have

$$\begin{cases} \begin{cases} F_{ix}^\tau = -\mu_i \cos\vartheta F_i^n \\ F_{iy}^\tau = -\mu_i \sin\vartheta F_i^n \end{cases} & \text{if } \sqrt{{v_{ix}^\tau}^2 + {v_{iy}^\tau}^2} \neq 0 \ \text{(slip)} \\ \sqrt{{F_{ix}^\tau}^2 + {F_{iy}^\tau}^2} \leq \mu_{s,i} F_i^n & \text{if } \sqrt{{v_{ix}^\tau}^2 + {v_{iy}^\tau}^2} = 0 \ \text{(stick)} \end{cases} \tag{4}$$

where ϑ gives the sliding direction, and μ_i and $\mu_{s,i}$ are respectively the slip and static friction coefficients at the point p_i.

Generally, the complementary conditions introduced above, combined with the equations for $\ddot{\boldsymbol{\delta}}$ and $\dot{\boldsymbol{v}}^\tau$, provide enough information for us to determine the contact forces. It is worth noting that $\boldsymbol{v}_i^\tau = 0$ is equivalent to a tangential constraint at the contact point p_i. In this case, use $\dot{v}_{ix}^\tau = \dot{v}_{iy}^\tau = 0$ as additional supplementary conditions to find the solutions of the contact forces [38,37]. In addition, the empirical law of Coulomb's friction may induce model singularities when two contacts are simultaneously engaged by the dimer. Resolution of this situation can be found in [43].

2.2 Impact dynamics

Once an impact occurs, its small time scale allows several hypotheses to be introduced: invariance of the system configuration, negligible non-impulsive forces, and separation of energy dissipations due to the normal and tangential motions at a contact point. Under these hypotheses, Eq. (2) can be simplified to the following form:

$$\boldsymbol{M}d\dot{\mathbf{q}} = \boldsymbol{W}d\boldsymbol{P}^n + \boldsymbol{N}d\boldsymbol{P}^\tau, \tag{5}$$

where $\boldsymbol{P}^n$ and $\boldsymbol{P}^\tau$ are respectively the normal and tangential impulses at the two contact points such that $d\boldsymbol{P}^n = \boldsymbol{F}^n dt$ and $d\boldsymbol{P}^\tau = \boldsymbol{F}^\tau dt$.

At the contact p_i, the work w_i done by the normal force F_i^n via a normal deformation δ_i satisfies $dw_i = F_i^n \cdot d\delta_i = \dot{\delta}_i dP_i^n$. The work induces variation in the elastic potential energy E_i.

Accumulation of the potential energy occurs during compression ($\dot{\delta} < 0$) by $dE_i = -dw_i$, while its release happens during restitution ($\dot{\delta} > 0$) along with dissipation by the factor of $1-e_i^2$, that is, $dw_i = -e_i^2 dE_i$, where e_i is a macroscopic parameter termed as the *energetic coefficient of restitution* [44]. This coefficient encapsulates the energy loss induced by various factors confined in a single compression-expansion cycle during impact. Note that a molecular dynamics technique [30,36] often adopts a viscous-force model scaled by a damping coefficient to consider the energy dissipation in impacts. Nevertheless, the intrinsic instability as well as possible uncertainty in the value of the damping coefficient may misleads numerical simulation to deviate from real physics.

The potential energy E_i also depends on the constitutive model for the normal contact force with respect to the relative deformation. Here, we assume $F_i^n = f_i(\delta_i) = k_i(-\delta_i)^{\eta_i}$, where, for $i = 1, 2$, k_i is the stiffness at p_i. The normal deformation δ_i is always negative to represent local compression. And η_i is an exponent depending on contact mechanics. We can obtain dF_i^n/dE_i from differentiating $F_i^n = k_i(-\delta_i)^{\eta_i}$ followed by a substitution $\delta_i = -(F_i^n/k_i)^{1/\eta_i}$. For details refer to [43]. Integration of dF_i^n/dE_i yields F_i^n as a function of E_i only.

Denote by E_j the larger value of E_1 and E_2 such that P_j^n is the *primary impulse*. For the dimer system, we assume Hertz contact with $\eta_i = 3/2$, and the same material property for the two contact points so $k_i/k_j = 1$. It follows that

$$\frac{dP_i^n}{dP_j^n} = \frac{F_i^n}{F_j^n} = \left(\frac{E_i}{E_j}\right)^{3/5} = \Lambda_{i,j}^n. \tag{6}$$

Note that Eq. (6) does not require any specific value of the contact stiffness k_i. This also prevails over the MD technique in which a concrete value must be specified to the contact stiffness. Depending upon the potential energy residing in each contact via the work w_i, the combination of the values of $\Lambda_{i,j}^n$ obtained from (6) presents an instantaneous distribution of the normal contact forces.

Under Coulomb friction, the differential tangential impulse dP_i^τ is related to the differential primary impulse dP_i^n in the same way as the tangential force to the normal force. Here, Eq. (6) further relates dP_i^τ to dP_j^n. This prompts us to choose P_j^n as a "time-like" independent variable, and rewrite (5) as

$$\boldsymbol{M} d\dot{\mathbf{q}} = (\boldsymbol{W}\boldsymbol{\Lambda}^n + \boldsymbol{N}\boldsymbol{\Lambda}^\tau) dP_j^n, \tag{7}$$

where $\boldsymbol{\Lambda}^n = [\Lambda_{1,j}^n, \Lambda_{2,j}^n]^T$ and $\boldsymbol{\Lambda}^\tau$ are the ratio matrices of all impulses, normal or tangential, relative to the primary impulse dP_j^n.

At the start of the impact, there is no potential energy and no impulses at either contact. For numerical simulation, the initial values for $\boldsymbol{\Lambda}^n(0)$ and $\boldsymbol{\Lambda}^\tau(0)$ are provided in [38]. Thus, the impact dynamics described by (7) can be advanced along with the normal impulse P_j^n, accompanied by timely updating of the values of $\boldsymbol{\Lambda}^n$ and $\boldsymbol{\Lambda}^\tau$. The impact at the contact p_i ends when $E_i = 0$. Multiple impacts finish when $E_1 = E_2 = 0$. As this condition is satisfied, the solution to (7) corresponds to the post-impact velocities of the system.

2.3 Classification of the contact/impact states

Despite only two potential contact points involved in the system, impact and friction can still trigger plenty of possible combinations of contact modes. We introduce the following three binary digits to quantify the contact mode at p_i, $i = 1, 2$:

$$\begin{aligned} a_i(\delta_i) &= \begin{cases} 1 \text{ if } \delta_i = 0 \\ 0 \text{ if } \delta_i > 0, \end{cases} \quad b_i(\dot{\delta}_i) = \begin{cases} 1 \text{ if } \dot{\delta}_i < 0 \\ 0 \text{ if } \dot{\delta}_i \geq 0, \end{cases} \\ c_i(|\boldsymbol{\upsilon}_i^\tau|) &= \begin{cases} 1 \text{ if } |\boldsymbol{\upsilon}_i^\tau| \neq 0 \\ 0 \text{ if } |\boldsymbol{\upsilon}_i^\tau| = 0. \end{cases} \end{aligned} \tag{8}$$

The variable $a_i(\delta_i)$ states whether contact is engaged or not, $b_i(\dot{\delta}_i)$ identifies the occurrence of an impact event, and $c_i(|\boldsymbol{\upsilon}_i^\tau|)$ describes stick or slip in the tangential direction. The contact mode at p_i can be represented by a triple $s_i = \langle a_i, a_i\&b_i, a_i\&c_i\rangle$. After bit operations, there exist five possible values for s_i, since the values of $b_i(\dot{\delta}_i)$ and $c_i(|\boldsymbol{\upsilon}_i^\tau|)$ make sense only if $a_i(\delta_i) = 1$. Refer to a combination of the modes at p_1 and p_2 as a *contact state*. Subsequently, we classify the motion of the dimer into twenty-five states shown in Table 1.

Table 1. Contact states possibly triggered in the motion of the bouncing dimer.

s_1 \ s_2	$\langle 0,0,0\rangle$	$\langle 1,0,0\rangle$	$\langle 1,0,1\rangle$	$\langle 1,1,0\rangle$	$\langle 1,1,1\rangle$
$\langle 0,0,0\rangle$	FM[1]	SC_{sk}[2]	SC_{sp}	SI_{sk}	SI_{sp}
$\langle 1,0,0\rangle$	SC_{sk}	$DC_{(sk,sk)}$	$DC_{(sk,sp)}$	$DI_{(sk,sk)}$	$DI_{(sk,sp)}$
$\langle 1,0,1\rangle$	SC_{sp}	$DC_{(sp,sk)}$	$DC_{(sp,sp)}$	$DI_{(sp,sk)}$	$DI_{(sp,sp)}$
$\langle 1,1,0\rangle$	SI_{sk}	$DI_{(sk,sk)}$	$DI_{(sk,sp)}$	$DI_{(sk,sk)}$	$DI_{(sk,sp)}$
$\langle 1,1,1\rangle$	SI_{sp}	$DI_{(sp,sk)}$	$DI_{(sp,sp)}$	$DI_{(sp,sk)}$	$DI_{(sp,sp)}$

[1]FM stands for Free Motion; SC for Contact at a Single point; SI for Impact at a Single point; DC for Contact at Double points; and DI Impact at Double points.
[2]Subscripts sk stands for friction in a stick state; and sp for friction in a slip state.

3 Periodic structures in the dimer's motion

In this section, we perform numerical simulation based on the nonsmooth model given in Sect. 2. Following [28], an aspect ratio $A_r = (l + 2r)/(2r)$ is used along with r to describe the geometry of the dimer, and a dimensionless acceleration $\Gamma = 4\pi^2 f^2 A_z/g$ along with $f = \omega/2\pi$ to represent the intensity of the vibration, where g is the gravitational acceleration.

Unless explicitly specified, all simulations are performed over a dimer comprising two steel spheres with radius $r =$ 5mm, density $\rho_b = 7.85 \times 10^3 \text{kg/m}^3$; and a plexiglass rod with diameter $D_r =$ 4mm and density $\rho_r = 1.18 \times 10^3 \text{kg/m}^3$. We also set the coefficients of restitution $e_1 = e_2 = 0.6$; the coefficients of friction for slip $\mu = 0.2$ and that for stick $\mu_s = 0.4$; and $A_r = 6$, $\Gamma = 0.9$ and $f =$ 15Hz. These parameters are mainly abstracted from [28] in which the dimer's dynamics is limited in a planar motion.

3.1 Normal motion and concatenation of contact states

We set the dimer's *initial configuration, i.e.*, its position and velocity at release down to the plate, as $\mathbf{q}(0) = (0, 0, r, 0, 4\pi/45, 0)^T$ and $\dot{\mathbf{q}}(0) = (1, 0, 0, 0, 0, 0)^T$. This corresponds to lifting the dimer to an incline angle $\beta(0) = 4\pi/45$ while keeping one of its ends on the plate. The dimer is released with a horizontal velocity $\dot{x}_1(0) = 1$ at the moment the plate is at its equilibrium position, *i.e.*, $\phi_0 = 0$.

Figure 2 shows that the vibrating plate excites the dimer to form a stable periodic motion, similar to the drift mode in 2D dynamics [28,37]. While ball B_1, referred to as the *contacting ball*, appears to be staying on the plate nearly all the time, and ball B_2, referred to as the *bouncing ball*, is bouncing in phase with the plate. We refer to [43] for the normal displacement diagrams of the jump mode, in which both ends bounce almost synchronously, and the flutter mode, in which both ends take turns to impact the plate with a time interval in between that is twice the vibration period.

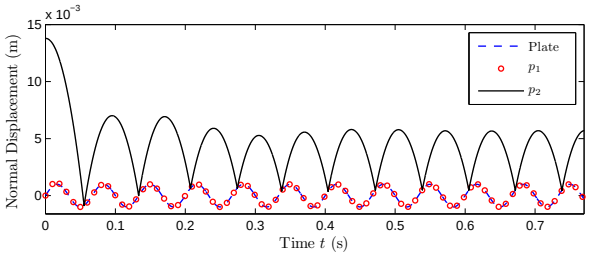

Fig. 2. (Color online) Normal displacements of the vibrating plate (blue dashed line), ball B_1 (red circles), and ball B_2 (black solid line) in the drift mode under $\dot{x}_1(0) = 1$, $A_r = 6$, $e = 0.6$, $\Gamma = 0.9$, $f = 15$Hz, $\mu = 0.2$, and $\mu_s = 0.4$.

Because of the discrete impact events, the motion of the bouncing dimer in each of the above three periodic modes is discontinuous. Moreover, Coulomb friction significantly complicates the impact processes due to possible stick-slip transitions within impact dynamics. Therefore, states $\mathrm{SI_{sp}}$ and $\mathrm{SI_{sk}}$ may occur together or separately during an event of single impact at B_1. Similarly, an event of double impacts may also consist of different contact states (see Table 1) subject to friction at each contact point.

Nevertheless, state transitions in each mode form a cycle. For the drift mode, every cycle begins with an event of double impacts, followed by a sequence of single impact events involving the contacting ball B_1. The sequence transfers into state $\mathrm{SC_{sp}}$ in which B_1 keeps contact with the vibrating plate while the bouncing ball B_2 stays in the air. The cycle ends with repeated events of double impacts, triggered by B_2's landing onto the plate. Under the parameters given in Fig. 2, the event of double impacts begins with state $\mathrm{DI_{(sp,sp)}}$, and gradually transfer into state $\mathrm{DI_{(sp,sk)}}$. This state is then maintained until the end of the double impacts.

Although the sequence of the state transitions in a cycle of the drift mode is complex, a detailed inspection through simulation indicates that an event of double impacts always occurs at the instant when the plate's motion is located in the first quadrant of the vibration cycle. In this case, the direction of the normal velocity at p_2 is opposite to that of the plate velocity, such that part of energy is transferred from the vibrating plate to the dimer via the double impacts. The succeeding events of single impact at p_1 plays a role of adjusting the energy that can be held in a stable drift mode of the dimer.

3.2 Periodic structures of phase portraits

If the event of double impacts in a drift mode ends with state $\mathrm{DI_{(sp,sk)}}$, not only does the normal motion of the bouncing dimer exhibit periodic pattern, but also our numerical simulation shows that the attitude angles θ, β, γ are periodic. We plot the phase trajectories of θ, β, γ by neglecting the duration that precedes the periodic drifting behavior.

Figure 3 depicts the phase trajectories in the β-$\dot{\beta}$ plane for the dip angle. In the drift mode, the phase trajectory corresponds to a stable limit cycle with a D-shape, asymmetric with respect to the origin of the phase plane. The vertical line in Fig. 3 corresponds to the event of double impacts that sharply changes the value of $\dot{\beta}$ through an ignorable time interval within which the contact state varies from $\mathrm{DI_{(sp,sp)}}$ (dots in the line) to $\mathrm{DI_{(sp,sk)}}$ (circles in the line).

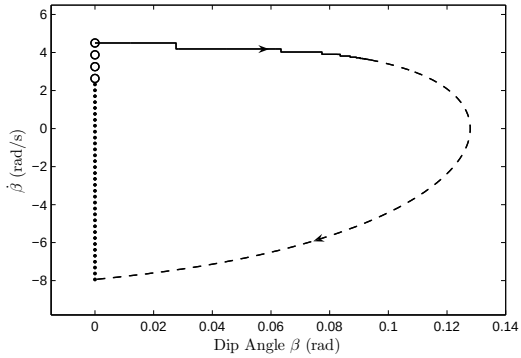

Fig. 3. Phase portrait of the dip angle β versus its changing rate in the drift mode under $\dot{x}_1(0) = 1$, $A_r = 6$, $e = 0.6$, $\Gamma = 0.9$, $f = 15$Hz, $\mu = 0.2$, and $\mu_s = 0.4$. Arrows along the orbits mark the phase evolution with time. The solid curve represents a phase composed of contact states FM and $\mathrm{SI_{sp}}$ (or $\mathrm{SI_{sk}}$). The dashed curve depicts state $\mathrm{SC_{sp}}$, while the dots and circles respectively depict states $\mathrm{DI_{(sp,sp)}}$ and $\mathrm{DI_{(sp,sk)}}$. The same representation will be used in the upcoming phase portraits.

The phase trajectory for the precession angle θ in the drift mode is shown in Fig. 4. It exhibits an asymmetric periodic structure, separated by the events of double impacts. Both single and double impacts have slight influence on the change in $\dot{\theta}$. The asymmetric structure mainly stems from coupling effects in the dimer's dynamics within states FM and $\mathrm{SC_{sp}}$.

The curve plotted in Fig. 5 for the spinning angle γ also exhibits periodicity with a nonzero mean. We can see that the value of $\dot{\gamma}$ changes little before and after an event of double impacts, but decreases dramatically when an event of single impact occurs.

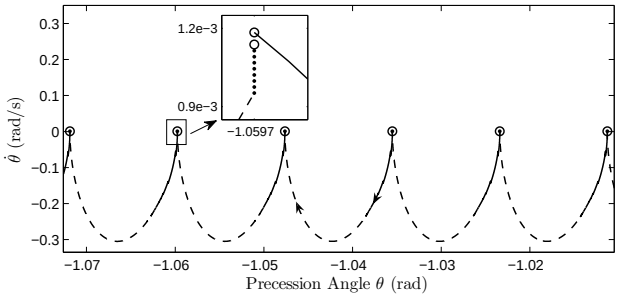

Fig. 4. Phase portrait of the precession angle θ versus its changing rate in the drift mode under $\dot{x}_1(0) = 1$, $A_r = 6$, $e = 0.6$, $\Gamma = 0.9$, $f = 15$Hz, $\mu = 0.2$, and $\mu_s = 0.4$. Inset related to a cuspid shows the process of the double impacts that change not only the value of $\dot{\theta}$, but also the contact state. Curves, dots, and circles carry the same meanings as in Fig. 3.

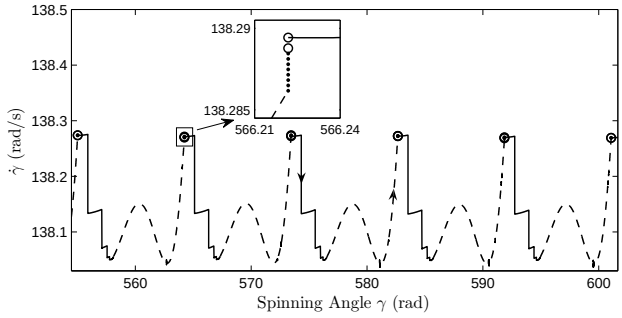

Fig. 5. Phase portrait of the spinning angle γ versus its derivative in the drift mode under $\dot{x}_1(0) = 1$, $A_r = 6$, $e = 0.6$, $\Gamma = 0.9$, $f = 15$Hz, $\mu = 0.2$, and $\mu_s = 0.4$. Inset presents the process of the double impacts that change not only the value of γ, but also the contact state. Curves, dots, and circles carry the same meanings as in Fig. 3.

3.3 Ratchet transport induced by periodic responses

Let us project the trajectory of the dimer's center of mass onto a horizontal plane, as shown in Fig. 6. A surprising behavior exists in the drift mode: the trajectory projection is globally circular with local fluctuations. A symmetry argument can be employed to explain how such motion pattern is formed. During a period T of the drift mode, the spinning rotation γ dominates the horizontal transport to generate a bias because of the asymmetry in the precession θ. This bias can be periodic through modulation of the asymmetry in the dip angle β to produce local fluctuations in response to the plate vibration. Therefore, the formation of a stable circular orbit basically comes from the following three factors: supply of energy periodically to the dimer through impacts by the vibrating plate; transfer of part of this energy to the dimer's horizontal motions via friction; and directed rotation of the dimer owing to the asymmetric structures in the variables of the dynamics.

4 Excitation of the drift mode

Excitation of the drift mode depends on the dimer's initial configuration, the plate's vibration intensity Γ and frequency f, the

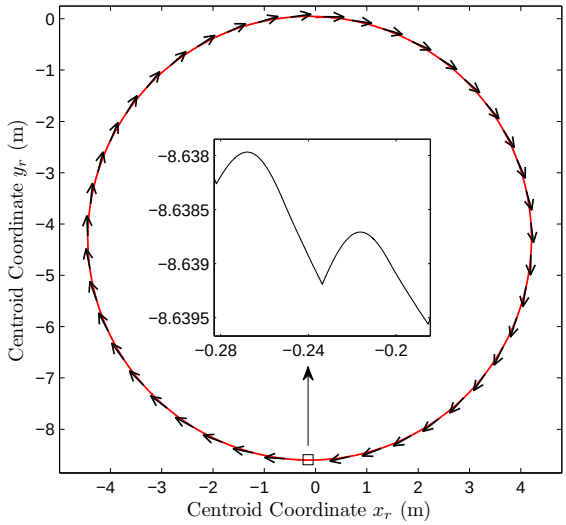

Fig. 6. Trajectory of the center of mass of the dimer projected onto a horizontal plane in the drift mode under $\dot{x}_1(0) = 1$, $A_r = 6$, $e = 0.6$, $\Gamma = 0.9$, $f = 15$Hz, $\mu = 0.2$, and $\mu_s = 0.4$. Arrows positioned along the orbits signify tangential velocities of the center of mass at some discrete instants. The inset presents an asymmetric and curved teeth structure.

aspect ratio A_r, as well as the physical parameters of impact and friction. To investigate the effect of these factors on the formation of the drift mode, here we look at a special scenario. The dimer is lifted at one end (p_2) with an incline angle $\beta(0)$ while its other end (p_1) rests on the plate. At the instant when the plate is at its equilibrium position, the dimer is released with a horizontal velocity $\dot{x}_1(0)$ perpendicular to its spinning axis. The initial configuration of the dimer is fully specified by $\beta(0)$ and $\dot{x}_1(0)$.

4.1 Initial configuration, vibration frequency, and aspect ratio

Numerical simulation has demonstrated that $\dot{x}_1(0)$ does not affect the sequence of contact states, thus has no effect on the formation of the drift mode. Therefore, the influence by the initial configuration over excitation of the drift mode mainly comes from the angle of inclination $\beta(0)$, which determines the initial energy of impacts. We denote by $\beta_d(0)$ a value of $\beta(0)$ that can excite a drift mode. Keeping $\dot{x}_1(0) = 1$, under different vibration frequencies, we study the distribution of $\beta(0)$ which can excite the drift mode in $(0, \pi/2)$.

Figure 7 presents intervals of $\beta_d(0)$ while β changes from 0 to $\pi/2$, under different vibration frequencies f. The distribution of available values $\beta_d(0)$ varies with the frequency. The gap between continuous intervals of $\beta_d(0)$ is sparse under a low frequency but gradually gets denser as the frequency increases. Nevertheless, the total length of the intervals of $\beta_d(0)$ varies little across different frequencies. This means the excitation of the drift mode is basically irrelevant to frequency, though different values of f can change the extent of $\beta_d(0)$ diffusing in $(0, \pi/2)$. From the numerical investigations, we may understand the experimental findings[28] that the formation of a drift mode in a

2D dimer can be easily triggered, but sensitively depends on the initial condition.

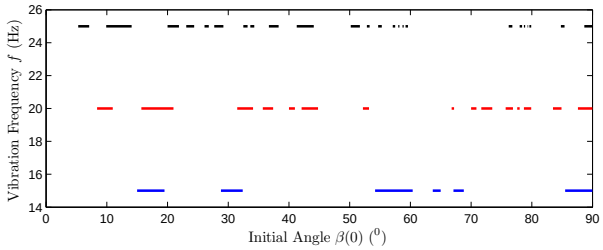

Fig. 7. (Color online) Distributions of the values of $\beta_d(0)$ capable of exciting a drift mode under vibration frequencies f = 15Hz (blue segments), 20Hz (red segments), and 25Hz (black segments). Here, $\dot{x}_1(0) = 1$, $A_r = 6$, $e = 0.6$, $\Gamma = 0.9$, $\mu = 0.2$, and $\mu_s = 0.4$.

As has been found in the experiments [28] and the numerical simulations [37] for a 2D dimer in a drift mode, the energy (only relevant to normal motion) per unit mass decreases with frequency, and is approximately $g/(8f^2)$. The finding also agrees with our numerical investigation into a 3D scenario in which the energy confined in a drift mode decreases with frequency. Consider the energy confined in the periodic normal motion is primarily related to the frequency f, and nearly unaffected by the initial energy scaled by the value of $\beta_d(0)$. This may have the implication of the drift motion with quantal features since its energy can be stabilized into a constant level relying mainly on f.

Once a value of $\beta_d(0)$ for a frequency f_1, now denoted as $\beta_{d|f_1}$ for clarity, is known, we can estimate a value $\beta_{d|f_2}(0)$ for another frequency f_2 according to the energy that can be confined in a drift mode. The above estimation, however, is valid only for the first interval of $\beta_{d|f_2}(0)$, because a complex transition stage before the formation of a drift mode would be triggered when $\beta(0)$ is relatively large.

According to our numerical results, the aspect ratio A_r has barely any effect over the excitation of the drift mode when the initial configuration of the dimer is adjustable. However, experiments [28] revealed that unstable drift mode would appear when $A_r < 2.5$. A possible explanation for that is given as follows. Note that the energy pumped into the dimer through the impact of the bouncing ball B_2 must be adjusted via a sequence of single impacts at ball B_1. As A_r decreases below certain threshold, ball B_1 cannot be stabilized on the vibrating plate before ball B_2 falls down to the plate. This means that new energy will be input into the dimer by the impact of B_2 before the process of energy adjustment via a sequence of single impacts at B_1 is accomplished. In this case, the dimer cannot reach the energy level to sustain a stable drift mode.

4.2 Coefficient of restitution and vibration intensity

The dimer could maintain periodic motions because of its ability to extract energy from the vibrating plate through frictional impacts during a modulated process. Basically, the vibration intensity Γ manages the compensation effect of energy, while the coefficient of restitution e captures the effect of energy dissipation. There should be a range of Γ within which the drift mode could always start for certain value of e. Based on numerical simulation, Fig. 8 plots the region R_1 of (e, Γ) that could activate the drift mode when $e \in (1/3, 4/5)$ under vibration frequency $f = 15Hz$. The range in R_1 is narrow, which agrees with the findings in [30] for studying the dynamics of a bouncing rod. Region R_2 corresponds to a dead zone, in which the dimer will eventually collapse down to the plate, and then maintain contact with it. Across the upper boundary of R_1, other modes, such as flutter, periodic-doubling bifurcation, and stochastic motions may be stimulated.

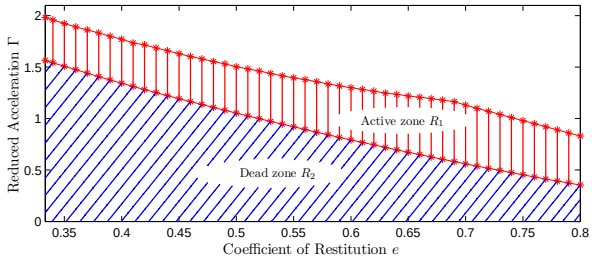

Fig. 8. (Color online) The e-Γ plane partitioned based on excitation of a drift mode under $\dot{x}_1(0) = 1$, $A_r = 6$, f = 15Hz, $\mu = 0.2$, and $\mu_s = 0.4$. Parameter values in R_1 (zone with red straight lines) can excite a drift mode over an appropriate initial condition, while in R_2 (zone with blue slashes) will make a dimer finally stay on the vibrated plate in any initial conditions. Complex behaviors appear in the region above R_1.

For a drift mode excited by a point (e, Γ) inside R_1, an event of double impacts appears to always occur at the instant when the vibration cycle is in the first quadrant. In addition, for given values of e and Γ, the phase angle in the vibration cycle, related to the event of double impacts, barely varies with other parameters once the drift mode is activated. If (e, Γ) lies in the dead zone R_2, however, the phase angle at the occurrence of an event of double impacts occurring will eventually enter into one of the other quadrants in the vibration cycle, which essentially cannot transfer energy via impacts to the dimer, thus causing it to a stop.

4.3 Coefficients of friction

Friction has little effect over the periodicity of the normal motion of the bouncing dimer, but significant influences over its horizontal transport behaviors due to different asymmetric structures for the slip motions at the contact points p_1 and p_2.

As experimentally discovered in [28] for the drift mode in the 2D dynamics, a small aspect ratio A_r will generate a *positive motion* drifting in a direction from the "contacting" end p_1 to the "bouncing" end p_2. While a large A_r will result in a *negative motion* along a direction pointing from p_2 to p_1. The difference between them, as shown in [37], is that a negative drift motion occurs because the slip velocity at p_1 disappears at the end of double impacts with a state $\mathrm{DI}_{(\mathrm{sk,sk})}$, while a positive

motion takes a positive post-impact slip velocity at p_1 larger than the one before these impacts.

Notice that these different phenomena are related to the distinct contact states ending in the events of double impacts. Also, these distinct contact states were triggered by setting dimers with different aspect ratio A_r and keeping friction coefficients unchanged. In fact, both the aspect ratio and the coefficient of friction can affect the contact state during double impacts, and thus change the property of the trajectory or the direction of the drift motion [37]. Therefore, for a dimer with a given value of A_r, similar phenomena can be realized by adjusting the values of friction coefficients.

Similar to the case of a 2D bouncing dimer, the drift mode for a 3D counterpart also exhibits different transport properties because of various behaviors of the slip motions that can be initiated by the event of double impacts. We have performed numerical simulation under $\mu = 0.05$ and $\mu_s = 0.1$ while keeping the values of the other parameters the same as in Sect. 3. The normal motions in both scenarios are nearly identical, while their slip motions at contact points (e.g., the horizontal velocity of p_1 in Fig. 9) clearly differ from each other. In particular, Fig. 10 shows that the drift mode in the case of small friction generates an inward spiral trajectory.

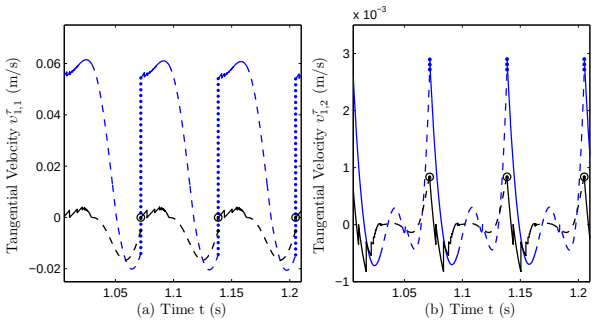

Fig. 9. (Color online) Under two sets of friction coefficients, the horizontal velocity $\boldsymbol{v}_1^{\tau}$ at the end p_1 has components (a) $v_{1,1}^{\tau}$ along the direction from the projection of p_1 to that of p_2, and (b) $v_{1,2}^{\tau}$ along the direction vertical to the one in $v_{1,1}^{\tau}$, in the horizontal plane. Curves (solid and dashed), dots, and circles the same meanings as in Fig. 3. Black and blue marks correspond to cases of $(\mu, \mu_s) = (0.2, 0.4)$ and $(0.05, 0.1)$, respectively. Other parameters in simulations are $\dot{x}_1(0) = 1$, $A_r = 6$, $e = 0.6$, $\Gamma = 0.9$, $f = 15$Hz.

The key difference between circular and spiral orbits lies in whether $\mathrm{DI}_{(\mathrm{sp,sk})}$ or $\mathrm{DI}_{(\mathrm{sp,sp})}$ can be activated at the end of an event of double impacts. Our numerical investigation indicates that a circular orbit can be formed only if the event ends in a state $\mathrm{DI}_{(\mathrm{sp,sk})}$. If the event of double impacts ends in state $\mathrm{DI}_{(\mathrm{sp,sp})}$, the periodic structures in the phase space of the angle variables is slightly influenced (see Fig. 11 for the spinning angle γ), then a spiral trajectory appears. Noting that the drift direction in 2D is also related to the contact states at the end of the double impacts, we can say that *negative* and *positive* drift motions in 2D correspond to a *circular* and *spiral* orbits in 3D. One should note that the 2D negative motion only triggers a state $\mathrm{DI}_{(\mathrm{sk,sk})}$ since state $\mathrm{DI}_{(\mathrm{sp,sk})}$ does not exist in the planar motion of a rigid dimer. Our numerical simulation reveals

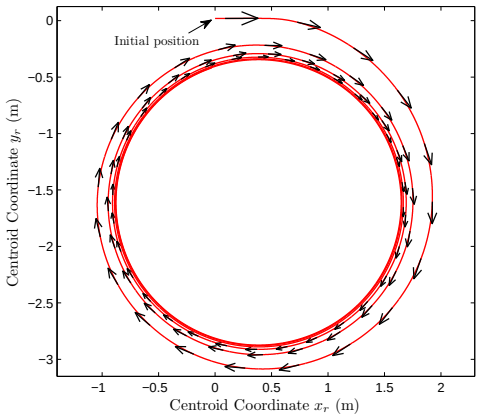

Fig. 10. (Color online) Trajectory (red solid line) of the dimer's center of mass projected onto the XY-plane under $\dot{x}_1(0) = 1$, $A_r = 6$, $e = 0.6$, $\Gamma = 0.9$, $f = 15$Hz, $\mu = 0.05$ and $\mu_s = 0.1$. Arrows positioned along the orbits represent the velocities of the center of mass at discrete instants. The length of each arrow is proportional to the magnitude of its represented center-of-mass velocity's tangential component.

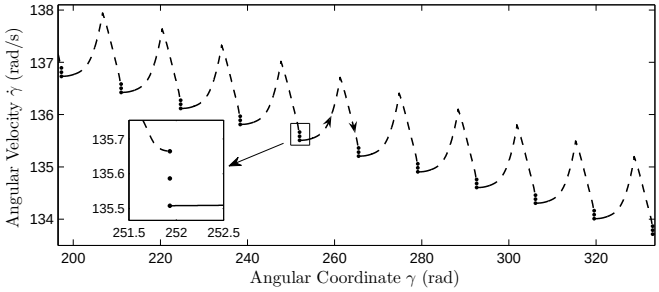

Fig. 11. Phase portrait $\dot{\gamma}$-γ in a drift mode under $\dot{x}_1(0) = 1$, $A_r = 6$, $e = 0.6$, $\Gamma = 0.9$, $f = 15$Hz, $\mu = 0.05$ and $\mu_s = 0.1$. Solid curves represent phases composed of contact states FM and $\mathrm{SI}_{\mathrm{sp}}$ (or $\mathrm{SI}_{\mathrm{sk}}$), dashed curves for state $\mathrm{SC}_{\mathrm{sp}}$, and dots for the mode $\mathrm{DI}_{(\mathrm{sp,sp})}$.

that state $\mathrm{DI}_{(\mathrm{sk,sk})}$ barely appears in a 3D drift motion unless a specific initial condition is designated to the dimer. If the state appears in a 3D drift mode, the orbit is also circular.

As shown in Fig. 9, the decrease of friction over the same A_r makes the contact state change from $\mathrm{DI}_{(\mathrm{sp,sk})}$ to $\mathrm{DI}_{(\mathrm{sp,sp})}$. Correspondingly, the circular orbit that can be formed with a given A_r may change into a spiral orbit when A_r decreases while friction remains unchanged.

Our numerical results also indicate that both the average velocities in precession angle and in orbit motion decrease as the dimer's center of mass follows an inward spiral trajectory. Note that the curvature of an inward spiral trajectory increases as the dimer moves. This means that the drift velocity decreases faster than the precession angular velocity $\dot{\theta}$. If an opposite situation exists, one may expect an outward spiral trajectory to be formed. However, this case does not appear in our numerical simulations.

Basically, unlocking the stick state in friction appears to play a damping effect which gradually decelerates the drift velocity to converge to a nearly constant value. This value cor-

responds to a circular orbit being gradually approached by the trajectory of the dimer's center of mass. This may be the reason why only an inward spiral trajectory can be formed when the double-impact event ends in a state $\mathrm{DI}_{(\mathrm{sp,sp})}$.

5 Circular orbit

Even though excitation of the drift mode and the characteristics of the circular orbit are influenced, to some extent, by all the parameters of dynamics, our numerical investigation indicates that the main parameters can be generally classified into the following two groups: (1) those that are mainly responsible for the excitation, including the coefficient of restitution e, the vibration intensity Γ, and the initial configuration of the dimer; and (2) those that dominate the properties of transport behaviors, including the aspect ratio A_r, the vibration frequency f, the coefficients of friction μ and μ_s, and the initial horizontal velocity $\dot{x}_1(0)$. In this section, we mainly focus on the circular orbit, along which excitation of the contact state $\mathrm{DI}_{(\mathrm{sp,sk})}$ in the stable drift motion is guaranteed by impacts with appropriate values of the frictional coefficients.

5.1 Orbit characteristics

The characteristics of a circular orbit include its radius, the period of the transport behavior, and the attitude of the dimer in the drift motion. Notice that the dimer in the drift mode has the same period T of the plate vibration. Each period contains only one event of double impacts. Suppose that such an event first occurs at t_1^- and then first vanishes at t_1^+. The same event in the ith cycle then ends at $t_i^+ = t_1^+ + (i-1)\,T$. At that time, the post-impact tangential velocity of the dimer's center of mass is $\bar{\boldsymbol{v}}_r^\tau(t_i^+)$, or simply, $\bar{\boldsymbol{v}}_r^\tau$.

Because the dimer at the instant t_i^+ assumes the configuration $\beta(t_i^+) = 0$, the direction of $\bar{\boldsymbol{v}}_r^\tau$ is tangent to the circular trajectory traced out by the dimer's center of mass at t_i^+, and its magnitude is constant owing to the periodic structures in the drift mode. By ignoring cyclic fluctuations induced by its bouncing motion, the dimer in the drift mode is equivalent to a moving particle with velocity $\bar{\boldsymbol{v}}_r^\tau$ along a circular orbit on a horizontal plane.

Denote by $\boldsymbol{e}_1$ the direction of the spinning axis of the dimer from the "contacting" end p_1 to the "bouncing" end p_2. The angle ζ between $\bar{\boldsymbol{v}}_r^\tau$ and $\boldsymbol{e}_1$ at the instant t_i^+ is

$$\zeta = \arccos\left(\frac{\bar{\boldsymbol{v}}_r^\tau \cdot \boldsymbol{e}_1(t_i^+)}{\|\bar{\boldsymbol{v}}_r^\tau\|}\right), \tag{9}$$

Here, ζ is limited in the scope $(0, \pi)$ as end p_1 is always inside of the circular orbit. Under the definition of ζ, the negative and positive drift motions in 2D is related to the situations $\zeta = \pi$ and $\zeta = 0$, respectively.

Actually, for the case of the 3D drift mode in an inward spiral orbit (see Fig. 10), we have $\zeta \in (0, \pi/2]$, in which p_1 points to p_2 in the moving direction. For the 3D drift mode with a closed circular orbit, we have $\zeta \in (\pi/2, \pi)$ in which p_2 is back to follow p_1 in the moving direction. For both cases, Fig. 12 details the scenarios of the dimer's attitude by its configuration relative to the instant when an event of double impacts occurs.

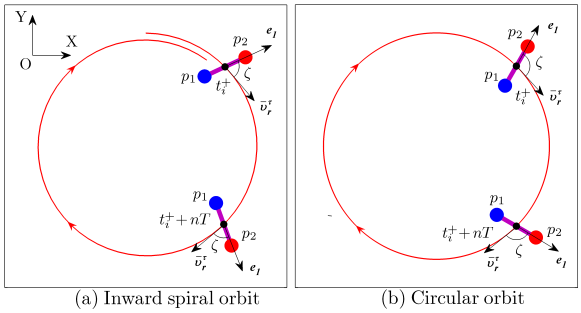

(a) Inward spiral orbit (b) Circular orbit

Fig. 12. (Color online) Attitude of the dimer in the drift mode relative to (a) an inward spiral orbit ($\zeta \le \pi/2$), and (b) a circular orbit ($\zeta > \pi/2$), respectively, at different instants when events of double impacts occur. Blue and red circles represent the "contacting" end p_1 and the "bouncing" end p_2, respectively.

Consider that the ratchet rotation is induced by a change in the precession angle θ, and confined in a periodic structure in the phase portrait of θ-$\dot{\theta}$. The average angular velocity of the ratchet rotation can be obtained by:

$$\bar{\omega}_\theta = \frac{1}{T}\int_{t_{i-1}^+}^{t_i^-} \dot{\theta}\, dt. \tag{10}$$

Neglecting cyclic fluctuations occurring in the interval of two adjacent events of double impacts, the equivalent radius of the circular orbit can be given as

$$\bar{R} = \frac{\|\bar{\boldsymbol{v}}_r^\tau\|}{|\bar{\omega}_\theta|}. \tag{11}$$

The uniform circular motion of the dimer in a drift mode allows the above expression to be characterized using an equivalent period $\bar{T}$:

$$\bar{T} = \frac{2\pi\bar{R}}{\|\bar{\boldsymbol{v}}_r^\tau\|} = \frac{2\pi}{|\bar{\omega}_\theta|}. \tag{12}$$

5.2 Effects of relevant parameters

We first look at the radius $\bar{R}$ of the circular orbit. Fix all the parameter values shown in the beginning of Sect. 3 except the initial horizontal velocity $\dot{x}_1(0)$. We slightly adjust the initial configuration to ensure the formation of a drift mode, then assign to $\dot{x}_1(0)$ a value within the interval $[0.5, 2.5]$. Fig. 13 presents the horizontal trajectories of the center of mass for different values of $\dot{x}_1(0)$. They are translated so that their centers coincide. The small variations in $\bar{R}$ suggests that the radius is almost independent of $\dot{x}_1(0)$.

Nevertheless, the value of $\bar{R}$ is significantly influenced by the aspect ratio A_r and the vibration frequency f. In particular, we found that $\bar{R} \propto (A_r - 1)^3$ (or equivalently, $\bar{R} \propto l^3$) and $\bar{R} \propto f^2$. The finding is confirmed by the numerical results shown in Fig. 14, which are obtained by varying the values of A_r and f, respectively, coupled with proper initial configurations to trigger the drift mode.

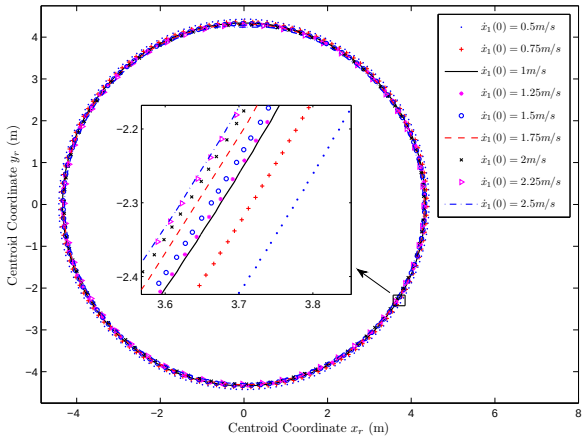

Fig. 13. (Color online) Projections of the center-of-mass trajectories onto the XY-plane with $\dot{x}_1(0)$ increasing from 0.5 to 2.5 under $A_r = 6$, $e = 0.6$, $\Gamma = 0.9$, $f = 15$Hz, $\mu = 0.2$, and $\mu_s = 0.4$. The inset details the trajectories in a very small time interval.

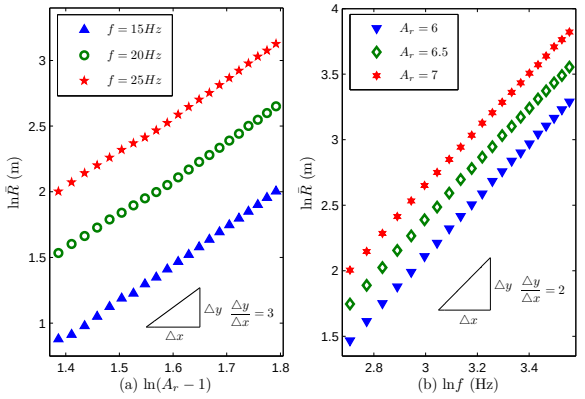

Fig. 14. (Color online) Variation trends of the equivalent radius $\bar{R}$ as affected by (a) the aspect ratio changing from $A_r = 5$ to 7, and (b) vibration frequency changing from $f = 15$ to 35Hz. Here, $\dot{x}_1(0) = 1$, $e = 0.6$, $\Gamma = 0.9$, $\mu = 0.2$, and $\mu_s = 0.4$.

Under the friction with coefficients $\mu = 0.2$ and $\mu_s = 0.4$, the formation of a circular orbit relies on a contact state $\mathrm{DI}_{(\mathrm{sp,sk})}$ that should appear at the end of a double-impact event. According to the qualitative analysis in [37], the occurrence of this state requires the aspect ratio to satisfy $A_r \geq 4.5$ when the friction is specified to the dimer's dynamics. The results in Fig. 14 are given for $A_r \geq 5$. Under $A_r = 5$ and $f = 15$Hz, the orbit radius takes on a value $\bar{R} \approx 2.4$m. For convenience of experimental realization, a smaller $\bar{R}$ is often needed. This can be implemented by adjusting friction such that a smaller A_r is permitted by a drift mode in a circular orbit. For instance, if friction is large enough to guarantee the event of double impacts ending in a state $\mathrm{DI}_{(\mathrm{sp,sk})}$, the radius of a circular orbit can be made less than 0.3m for the dimer with an aspect ratio $A_r = 4$ realized with the sphere radius $r = 2$mm and the distance $l = 12$mm between the two spheres.

Likewise, we can simulate the effects of A_r and f on the period $\bar{T}$ of the circular orbit and the attitude angle ζ. As shown in Fig. 15, when one of f and A_r is fixed, $\bar{T}$ scales with the other. However, ζ decreases very little monotonically around $\pi/2$ as A_r or f increases when $\dot{x}_1(0) = 1$. See Fig. 16.

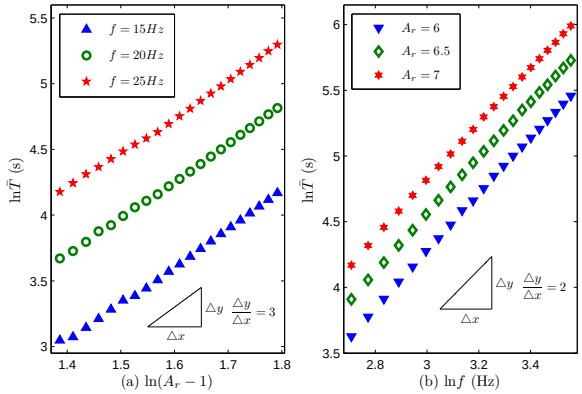

Fig. 15. (Color online) Period $\bar{T}$ increases as, (a) aspect ratio changes from $A_r = 5$ to 7, and (b)frequency changes from $f = 15$ to 35Hz, under $\dot{x}_1(0) = 1$, $e = 0.6$, $\Gamma = 0.9$, $\mu = 0.2$, and $\mu_s = 0.4$.

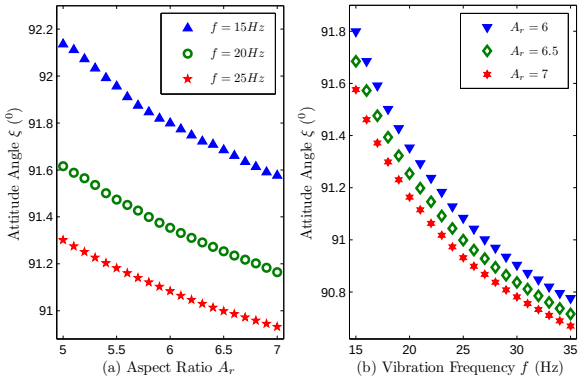

Fig. 16. (Color online) Attitude angle ζ decreases very little as: (a) aspect ratio changes from $A_r = 5$ to 7, and (b) frequency changes from $f = 15$ to 35Hz, under $\dot{x}_1(0) = 1$, $e = 0.6$, $\Gamma = 0.9$, $\mu = 0.2$, and $\mu_s = 0.4$.

Because both $\bar{T}$ and $\bar{R}$ are proportional to $(A_r - 1)^3$ and to f^2, from (11) and (12) we infer that $\bar{v}_r^\tau$ is independent of both A_r and f. Consider that $\bar{v}_r^\tau$ represents the transport velocity in the ratchet rotation. It is obviously related to the initial horizontal velocity $\dot{x}_1(0)$. Because $\bar{R}$ is independent of $\dot{x}_1(0)$, $\bar{T}$ and ζ will change with $\dot{x}_1(0)$.

Keeping all the parameters unchanged in simulation except the initial conditions, Fig. 17 presents how $\bar{T}$ and ζ vary with $\dot{x}_1(0)$. For a given A_r, the dimer moves in a similar circular orbit with a period $\bar{T}$ that can be minimized by tuning $\dot{x}_1(0)$. Under this case, the corresponding attitude angle ζ is close to $\pi/2$. See Fig. 17.

We have also performed numerical simulation to discover the influence of the intensity of the plate's vibration, the coef-

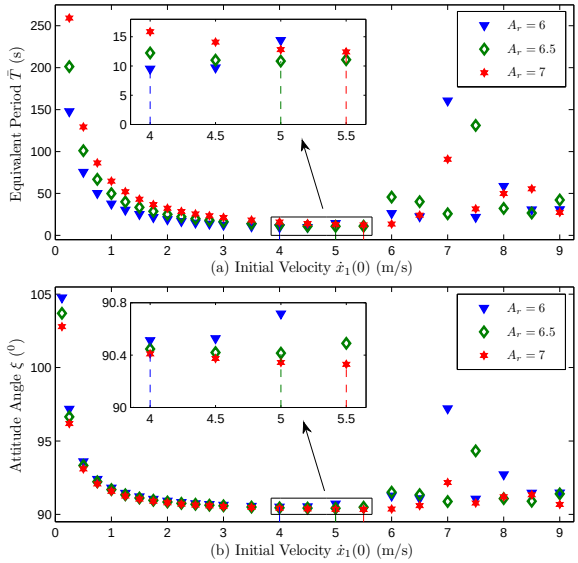

Fig. 17. (Color online) Variation of (a) orbit period $\bar{T}$, and (b) attitude angle ζ, as initial velocity changes from $\dot{x}_1(0) = 0.5$ to 9, under $e = 0.6$, $\Gamma = 0.9$, $f = 15Hz$, $\mu = 0.2$, and $\mu_s = 0.4$.

ficient of restitution and friction coefficients, on the characteristics of the circle orbit. If a circular orbit can be formed, these parameters have little effect on the values of $\bar{R}$, $\bar{T}$ and ζ.

6 Conclusion

In conclusion, we have performed comprehensive simulation to investigate the dynamics of a dimer bouncing on a vibrating plate. Despite the fact that the dynamics is complex with impacts and friction, the bouncing dimer under appropriate initial conditions and driving parameters reveals an intriguing pattern as a circular orbit traced by the center of mass of the dimer when projected onto a horizontal plane.

Through systematic simulation, we have discovered that excitation of the drift mode is mainly influenced by the coefficient of restitution e, the vibration intensity Γ, and the initial configuration of the dimer. A region in the e-Γ plane responsible for excitation of this mode is also numerically obtained. Friction significantly influences the behaviors of the ratchet rotation since it determines the shape of the asymmetric structure appearing in the slip motion of the dimer's contacting end. However, it has trivial effect on the excitation of the drift mode. Discussion is offered on the sensitivity of the circle-orbit mode to the initial configuration.

The characteristics of a closed circular orbit are mainly determined by several parameters, including the aspect ratio A_r, the vibration frequency f, and the initial horizontal velocity $\dot{x}_1(0)$. We find that the orbit radius $\bar{R}$ is closely proportional to $(A_r - 1)^3$ and f^2, and barely influenced by other parameters. The orbit period $\bar{T}$ is not only proportional to $(A_r - 1)^3$ and f^2, but also affected by $\dot{x}_1(0)$. In particular, the minimal period can be reached by tuning the value of $\dot{x}_1(0)$, and the corresponding attitude angle ζ is close to $\pi/2$.

Based on the numerical results, we have discovered that occurrences of the transport behaviors can be tracked back to the crucial event of double impacts. This event plays a dominant role in adjusting the energy confined in the bouncing dimer, and directing the ratchet motions through Coulomb friction. Though the dimer's dynamics is very complex due to collisions and friction, it seems that the dimer's motion in a drift mode can be further simplified as a particle moving in a circle with a uniform velocity. In the future, theoretical analysis of the property of the double impacts and experimental realization are expected for more deeply understanding the ratchet rotation exhibited in the 3D bouncing dimer, and furthermore, for discovering the physical mechanisms underlying in the vortices commonly observed in granular matter.

Appendix A Matrices for the dimer's dynamics

This appendix lists the forms of some matrices used in Sects 2.1 and 2.2 for the dynamics of the dimer system:

$$\boldsymbol{W} = \begin{bmatrix} 0 & 0 & 1 & 0 & 0 & 0 \\ 0 & 0 & 1 & 0 & lc_\beta & 0 \end{bmatrix}^T, \tag{A.1}$$

where symbols $s_{(\cdot)}$ and $c_{(\cdot)}$ are the abbreviations for trigonometric functions $\sin(\cdot)$ and $\cos(\cdot)$, respectively.

$$\boldsymbol{S}^\tau = \left[S^\tau_{1x},\ S^\tau_{2x},\ S^\tau_{1y},\ S^\tau_{2y} \right]^T, \tag{A.2}$$

where $S^\tau_{1x} = -rc_\theta\dot{\theta}\dot{\beta} + rs_\beta c_\theta\dot{\beta}\dot{\gamma} + rc_\beta s_\theta\dot{\theta}\dot{\gamma}$, $S^\tau_{2x} = (2ls_\beta - r)c_\theta\dot{\theta}\dot{\beta} + rs_\beta c_\theta\dot{\beta}\dot{\gamma} + rc_\beta s_\theta\dot{\theta}\dot{\gamma} + lc_\beta s_\theta(\dot{\theta}^2 + \dot{\beta}^2)$, $S^\tau_{1y} = -rs_\theta\dot{\theta}\dot{\beta} + rs_\beta s_\theta\dot{\beta}\dot{\gamma} - rc_\beta c_\theta\dot{\theta}\dot{\gamma}$, $S^\tau_{2y} = (2ls_\beta - r)s_\theta\dot{\theta}\dot{\beta} + rs_\beta s_\theta\dot{\beta}\dot{\gamma} - rc_\beta c_\theta\dot{\theta}\dot{\gamma} - lc_\beta c_\theta(\dot{\theta}^2 + \dot{\beta}^2)$,

$$\boldsymbol{N} = \begin{bmatrix} 1 & 1 & 0 & 0 \\ 0 & 0 & 1 & 1 \\ 0 & 0 & 0 & 0 \\ 0 & -lc_\theta c_\beta & 0 & -ls_\theta c_\beta \\ -rs_\theta & (ls_\beta - r)s_\theta & rc_\theta & (r - ls_\beta)c_\theta \\ -rc_\theta c_\beta & -rc_\theta c_\beta & -rs_\theta c_\beta & -rs_\theta c_\beta \end{bmatrix}, \tag{A.3}$$

$$\boldsymbol{M} = \begin{bmatrix} m & 0 & 0 & M_{14} & M_{15} & 0 \\ 0 & m & 0 & M_{24} & M_{25} & 0 \\ 0 & 0 & m & 0 & \frac{1}{2}mlc_\beta & 0 \\ M_{14} & M_{24} & 0 & M_{44} & 0 & J_2 s_\beta \\ M_{15} & M_{25} & \frac{1}{2}mlc_\beta & 0 & M_{55} & 0 \\ 0 & 0 & 0 & J_2 s_\beta & 0 & J_2 \end{bmatrix}, \tag{A.4}$$

where $M_{14} = -\frac{1}{2}mlc_\beta c_\theta$, $M_{15} = \frac{1}{2}mls_\beta s_\theta$, $M_{24} = -\frac{1}{2}mlc_\beta s_\theta$, $M_{25} = -\frac{1}{2}mls_\beta c_\theta$, $M_{44} = (\frac{1}{4}ml^2 + J_1)c^2_\beta + J_2 s^2_\beta$, $M_{55} = \frac{1}{4}ml^2 + J_1$, m is the total mass of the dimer, and J_1, J_2 are respectively the principal inertiaes of the dimer with respect to its center of mass along the axes $\boldsymbol{e}_1$ and $\boldsymbol{e}_2$ which is the unit vector of $\overrightarrow{O'Y'}$,

$$\boldsymbol{h}(\mathbf{q},\dot{\mathbf{q}},t)=\begin{bmatrix} -\frac{ml}{2}\left(c_\beta s_\theta(\dot\theta^2+\dot\beta^2)+2s_\beta c_\theta\dot\theta\dot\beta\right) \\ \frac{ml}{2}\left(c_\beta c_\theta(\dot\theta^2+\dot\beta^2)-2s_\beta s_\theta\dot\theta\dot\beta\right) \\ \frac{ml}{2}s_\beta\dot\beta^2 \\ \left((2J_1-2J_2+\frac{ml^2}{2})s_\beta\dot\theta-J_2\dot\gamma\right)c_\beta\dot\beta \\ -\left((J_1-J_2+\frac{ml^2}{4})s_\beta\dot\theta-J_2\dot\gamma\right)c_\beta\dot\theta \\ -J_2c_\beta\dot\theta\dot\beta \end{bmatrix}, \quad \text{(A.5)}$$

$$\boldsymbol{Q}=\begin{bmatrix}0 & 0 & -mg & 0 & -\frac{1}{2}mglc_\beta & 0\end{bmatrix}^T. \quad \text{(A.6)}$$

References

1. Z. A. Daya, E. Ben-Naim, R. E. Ecke, Eur. Phys. J. E **21**, (2006) 1–10.
2. V. Yadav, A. Kudrolli, Eur. Phys. J. E **35**, (2012) 1–7.
3. T. Mullin, Rhys. Rev. Lett. **84**, (2000) 4741–4744.
4. D. L. Blair, T. Neicu, A. Kudrolli, Phys. Rev. E **67**, (2003) 031303.
5. I. J. Aranson, L. S. Tsimring, Phys. Rev. E **67**, (2003) 021305.
6. I. Goldhirsch, G. Zanetti, Phys. Rev. Lett. **70**, (1993) 1619–1622.
7. James B. Knight, H. M. Jaeger, Sidney R. Nagel, Phys. Rev. Lett. **70**, (1993) 3728–3731.
8. Z. Farkas, P. Tegzes, A. Vukics, T. Vicsek, Phys. Rev. E. **60**, (1999) 7022–7031.
9. M. Levanon, D. C. Rapaport, Phys. Rev. E. **64**, (2001) 011304.
10. Z. Farkas, F. Szalai, D. E. Wolf, T. Vicsek, Phys. Rev. E. **65**, (2002) 022301.
11. A. J. Bae, W. A. M. Morgado, J. J. P. Veerman, G. L. Vasconcelos, Physica A: Statistical Mechanics and its Applications **342**, (2004) 22–28.
12. S. Collins, A. Ruina, R. Tedrake, M. Wisse, Science **307**, (2005) 1082–1085.
13. M. Gomes, A. Ruina, Phys. Rev. E **83**, (2011) 032901.
14. K. Lynch, C. K. Black, IEEE Trans. Robot. Automat. **17**, (2001) 113–124.
15. A. Mehta, J. M. Luck, hys. Rev. Lett. **63**, (1990) 393–396.
16. J. J. Barroso, M. V. Carneiro, E. E. N. Macau, Phys. Rev. E **79**, (2009) 026206
17. J. J. Barroso, M. V. Carneiro, E. E. N. Macau, Phys. Rev. E **79**, (2009) 026206.
18. T. Gilet, N. Vandewalle, S. Dorbolo, Phys. Rev. E **79**, (2009) 055201.
19. N. B. Tufillaro, T. M. Mello, Y. M. Choi, A. M. Albano, J. Phys **47**, (1986) 1477–1482.
20. J. M. Luck, Anita Mehta, Phys. Rev. E **48**, (1993) 3988–3997.
21. S. Giusepponi, F. Marchesoni, Europhys. Lett **64**, (2003) 36–42.
22. Z. J. Kowalik, M. Franaszek, P. Pieranski, Phys. Rev. A **37**, (1988) 4016–4022.
23. M. C. Vargas, D. A. Huerta, V. Sosa, Am. J. Phys. **77**, (2009) 857–861.
24. S. von Gehlen, M. Evstigneev, P. Reimann, Phys. Rev. E **79**, (2009) 031114.
25. D. Speer, R. Eichhorn, M. Evstigneev, P. Reimann, Phys. Rev. E **85**, (2012) 061132.
26. V. Frette, K. Christensen, A. Malthe-Sørenssen, J. Feder, T. Jøssang, P. Meakin, Nature **379**, (1996) 49–52.
27. D. Volfson, A. Kudrolli, L. S. Tsimring, Phys. Rev. E **70**, (2004) 051312.
28. S. Dorbolo, D. Volfson, L. Tsimring, A. Kudrolli, Phys. Rev. Lett. **95**, (2005) 044101.
29. J. Atwell, J. S. Olafsen, Phys. Rev. E **71**, (2005) 062301.
30. H. S. Wright, Michael R. Swift, P. J. King, Phys. Rev. E **74**, (2006) 061309
31. A. Kudrolli, G. Lumay, D. Volfson, L. S. Tsimring, Phys. Rev. Lett. **100**, (2008) 058001
32. S. Dorbolo, F. Ludewig, N. Vandewalle, New J. Phys. **11**, (2009) 033016.
33. K. Harth, U. Kornek, T. Trittel, U. Strachauer, S.Höme, K. Will, R. Stannarius, Phys. Rev. Lett. **110**, (2013) 144102
34. H.J. Herrmann, S' Luding, Continuum Mech. Thermodyn. **10**, (1998) 189.
35. S. Luding, Phys. Rev. E **52**, (1995) 4442.
36. E. Falcon, C. Laroche, S. Fauve, C. Coste, Eur. Phys. J. B, **5**, (1998) 111–131.
37. Z. Zhao, C. Liu, B. Brogliato, Proc. R. Soc. A **465**, (2009) 2267–2292.
38. C. Liu, Z. Zhao, B. Brogliato, Proc. R. Soc. A **464**, (2008) 3193–3211.
39. C. Liu, Z. Zhao, B. Brogliato, Proc. R. Soc. A **465**, (2009) 1–23.
40. Z. Zhao, C. Liu, B. Brogliato, Phys. Rev. E **78**, (2008) 031307.
41. C. Liu, H. Zhang, Z. Zhao, B. Brogliato, Proc. R. Soc. A **469**, (2013) 20120741.
42. H. Zhang, C. Liu, Z. Zhao, B. Brogliato, Sci. China-Phys. Mech. Astron. **56**, (2013) 875–881.
43. J. Wang, C. Liu, Z. Zhao, Multibody Syst. Dyn., Doi: 10.1007/s11044-013-9385-4.
44. W. J. Stronge, *Impact mechanics* (Cambridge University Press, 2000).